


Ab-initio simulations of coherent phonon-induced pumping of carriers in zirconium pentatelluride

Tao Jiang ¹, Peter P. Orth ^{1,2,3}, Liang Luo¹, Lin-Lin Wang ¹, Feng Zhang^{1,2}, Cai-Zhuang Wang^{1,2}, Jin Zhao^{4,5,6,7}, Kai-Ming Ho^{1,2}, Jigang Wang^{1,2} & Yong-Xin Yao ^{1,2}✉

Laser-driven coherent phonons can act as modulated strain fields and modify the adiabatic ground state topology of quantum materials. Here we use time-dependent first-principles and effective model calculations to simulate the effect of the coherent phonon induced by strong terahertz electric field on electronic carriers in the topological insulator ZrTe₅. We show that a coherent A_{1g} Raman mode modulation can effectively pump carriers across the band gap, even though the phonon energy is about an order of magnitude smaller than the equilibrium band gap. We reveal the microscopic mechanism of this effect which occurs via Landau-Zener-Stückelberg tunneling of Bloch electrons in a narrow region in the Brillouin zone center where the transient energy gap closes when the system switches from strong to weak topological insulator. The quantum dynamics simulation results are in excellent agreement with recent pump-probe experiments in ZrTe₅ at low temperature.

¹Ames National Laboratory, U.S. Department of Energy, Ames, IA, USA. ²Department of Physics and Astronomy, Iowa State University, Ames, IA, USA. ³Department of Physics, Saarland University, Saarbrücken, Germany. ⁴ICQD/Hefei National Laboratory for Physical Sciences at Microscale, and Key Laboratory of Strongly-Coupled Quantum Matter Physics, Chinese Academy of Sciences, Hefei, China. ⁵Department of Physics, University of Science and Technology of China, Hefei, China. ⁶Department of Physics and Astronomy, University of Pittsburgh, Pittsburgh, PA, USA. ⁷Synergetic Innovation Center of Quantum Information & Quantum Physics, University of Science and Technology of China, Hefei, China. ✉email: ykent@iastate.edu

Coherent phonons that are excited by laser pulses in the Terahertz (THz) or mid-infrared frequency range^{1–3} can provide nonthermal pathways for the dynamical control of quantum phases of condensed matter^{4–7}. Recent experimental demonstrations include ultrafast phononic manipulation of magnetic orders^{8–10}, of insulator-to-metal phase transitions^{11–13}, and a transient enhancement of martensitic phase¹⁴ and superconducting correlations^{15–18}. In topological quantum materials, coherent phonon excitations were shown to induce dynamical switching between different topological phases by modifying the crystal symmetry and by tuning strain fields^{19–27}. Particularly, recent coherent phonon pumping work provides compelling evidence of light-induced Dirac points²⁵, Weyl nodes²⁶ and enhanced stability of topological systems^{28,29}.

The theoretical understanding and first-principles simulations of light-excited electron-ion quantum systems are challenging, but significant progress has been achieved in recent years^{30–34}. Specifically to describe the ultrafast electronic and spin dynamics associated with phonon excitations, microscopic theories have been developed for the light-induced insulator-to-metal structural phase transition³⁵, the switching of magnetic orders³⁶, and the enhancement of superconducting correlations through symmetry-allowed electron-phonon coupling^{37–46}. Here, we theoretically investigate the switching between strong and weak topological insulators (STI and WTI) induced by THz-driven coherent Raman phonon excitations in the model Dirac system ZrTe_5 ²⁵. Although a qualitative picture has previously been established using static density functional theory (DFT) calculations²⁵, the ultrafast dynamics of the laser-driven system such as the observed continuous increase of electronic carrier density after the THz pump and the underlying mechanism, calls for more in-depth quantum dynamics simulations. The progress in this direction is highly appealing to the experimental community, who have been actively pursuing THz-driven quantum dynamics in various quantum materials recently^{47–50}.

In this paper, we simulate the coherent phonon-induced carrier dynamics in ZrTe_5 in the framework of time-dependent Schrödinger equation with DFT basis functions. We complement the DFT-based dynamics simulations by an effective model calculations that captures the essentials of the microscopic mechanism. Our detailed numerical analysis shows that the switching between STI and WTI, which necessarily involves the closing of the bulk gap, creates a small but finite volume in momentum space, where effective two-level systems (TLSs) undergo avoided level crossings. This results in Landau-Zener-Stückelberg (LZS) tunnelling^{51–56} and leads to an increase of the carrier concentration during several cycles of the coherent phonon modulation. Our time-dependent Schrödinger equation simulations predict the dynamics of the phonon-induced carrier concentration in quantitative agreement with the experiment.

Results and discussion

Summary of previous pump-probe experimental results. To facilitate the presentation, we summarize the key results of the THz pump-THz probe experiment on ZrTe_5 at 4.2 K, which is described in detail in Ref. ²⁵. These results motivate the numerical simulations in this work. In the experiment, an intense THz-pump pulse with an E -field trace plotted in Fig. 1a is incident normally on the ZrTe_5 single crystal. The THz pump-induced coherent phonon emission from the sample is observed after the pump pulse between $2.5 \text{ ps} \lesssim t \lesssim 5.8 \text{ ps}$, as highlighted in Fig. 1b. The coherent phonon emission lasts for about five full cycles and its dominant spectral peak at $f_{\text{ph}} = 1.2 \text{ THz}$ after Fourier transformation matches the A_{1g} Raman mode at the Brillouin zone center. By performing THz pump and THz probe measurements

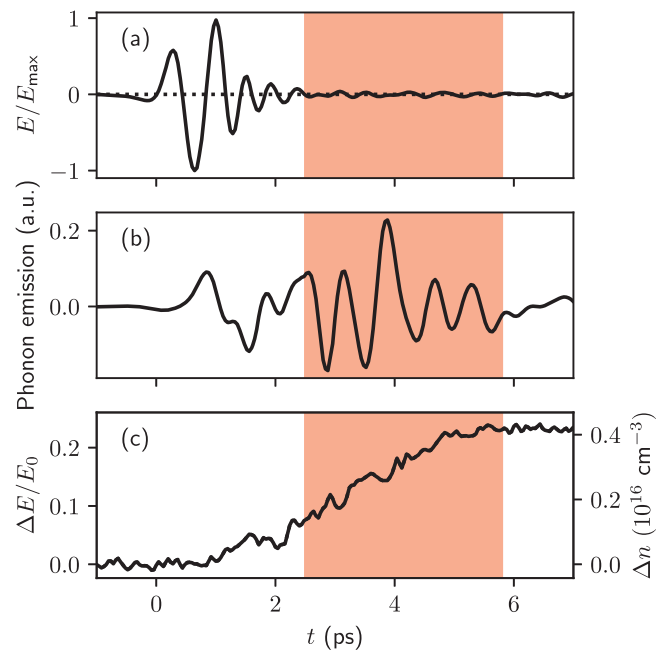


Fig. 1 THz pump-THz probe experimental results of ZrTe_5 at 4.2 K.

a Normalized THz pump E -field as a function of pump delay time t , with the maximal value of $E(t)$ being $E_{\text{max}} = 736 \text{ kV/cm}$. **b** Phonon emission as a function of t . The time-period after the pump pulse, where a coherent phonon emission is observed, is highlighted in red. This region is the focus of this work. **c** Normalized THz probe differential transmission $\Delta E(t)/E_0$ as a function of t . $\Delta E(t)$ is the differential transmission of the THz probe peak field E_0 measured with and without the THz pump pulse. The right y-axis labels the corresponding change of the carrier density Δn in unit of 10^{16} cm^{-3} .

using the same pump pulse, the THz probe differential transmission $\Delta E/E_0$, which is proportional to the change of carrier density Δn , is obtained and plotted in Fig. 1c. The carrier density continuously increases after the pump pulse as long as the coherent phonon emission is observed. It saturates for $t \gtrsim 5.8 \text{ ps}$, which coincides with the loss of phonon coherence. $\Delta E/E_0$ decays back to zero after about 120 ps²⁵.

In this paper, we focus on simulating this intriguing carrier excitation dynamics for the time period $2.5 \text{ ps} \lesssim t \lesssim 5.8 \text{ ps}$, where the coherent phonon excitation is present. The residual pump pulse is negligible during this time period, and the coherent phonon excitation can be treated as preexisting, i.e., without explicitly modelling the light-driven phonon generation process. The strong correlation between the carrier generation and the coherent phonon emission suggests a charge excitation mechanism assisted by a coherent Raman vibration. Indeed, by adiabatically following the A_{1g} phonon trajectory, static DFT calculations have revealed that the electronic state of the system undergoes a topological transition between STI to critical Dirac point (DP) to WTI²⁵ (see also Methods). This suggests the importance of the associated closing of the bulk band gap and potentially further topological effects in the carrier pumping process²⁵. This makes a detailed quantum dynamics simulations of the physical process highly desirable.

Effective model description

Model setup. We first study a toy model that qualitatively captures the dynamical carrier generation observed experimentally in ZrTe_5 . This model includes the essential physics underlying this phenomenon which is the topological phase transition (driven by coherent phonon oscillations) and a resulting inter-band charge

excitation. For simplicity, we consider a Kitaev chain model⁵⁷, which in momentum space is represented by the following two-orbital spinless fermion Bogoliubov-de Gennes (BdG) Hamiltonian:

$$H(k) = (-2\nu \cos(k) - \mu)\tau_z + 2\Delta \sin(k)\tau_y. \quad (1)$$

Here τ_i are the Pauli matrices and the Hamiltonian parameters include onsite energy μ , nearest-neighbor hopping ν and a superconducting pairing amplitude Δ . The momentum lies in the range $k \in [-\pi, \pi]$. The model obeys particle hole symmetry $\tau_x H^*(-k) \tau_x = -H(k)$.

With the chemical potential fixed at zero, the model exhibits a topological phase transition from a gapped superconductor that is trivial to one that is topological by tuning μ . The corresponding BdG band structures together with the orbital (τ_z) projections of the wavefunction are shown in Fig. 2a–e. This evolution of the band energies is qualitatively similar to the phonon-induced topological phase transition in ZrTe₅ obtained from DFT calculations^{25,58}. The band structure in panels (a) to (d) are obtained for μ/ν equal to $-2.02, -2.00, -1.97$ to -1.92 (a–d). The evolution of the band gap as a function of μ/ν is shown in panel (e). The bands in panels (a–d) are plotted together with weight of the projection of the Bloch wave function onto the first basis orbital ($\tau_z = 1$), as given by the size of the red circles. Clearly, a band inversion occurs when the system transforms from the trivial phase ($\mu/\nu < -2$) to the topological phase ($\mu/\nu > -2$). At $\mu/\nu = -2$, the band gap closes and a nodal point forms at Γ point. Consistently, the topological index, which can be defined as $Q \equiv \text{sign}(\mu^2 - 4\nu^2)$ ⁵⁷, is 1 in the trivial and -1 in

the topological phase, as labelled in panels (a,c,d). For the numerical simulations, we set $\nu = 1$ eV, and $\Delta/\nu = 0.1$, which results in a mode speed $\partial \epsilon_k / \partial k = \pm 2\Delta$ at the Dirac point ($\mu/\nu = -2$) that is in qualitative agreement with the Fermi velocity in ZrTe₅ when driven to DP by the A_{1g} phonon.

To model the effect of the coherent phonon excitation in ZrTe₅, we consider a periodic modulation of the onsite energy which resembles the treatment of electron–phonon coupling in the Holstein model⁵⁹:

$$\mu(t) = \mu_0 + \mu_1 \sin[\omega(t - t_0)] \quad (2)$$

resulting in the time-dependent Hamiltonian

$$H(k, t) = [-2\nu \cos(k) - \mu(t)]\tau_z + 2\Delta \sin(k)\tau_y. \quad (3)$$

We choose $\omega/2\pi = 1.2$ THz ($T = 833$ fs, $\hbar\omega = 4.96$ meV) to match the experimental value of the A_{1g} Raman mode frequency. We set $\mu_0/\nu = -1.97$ and $\mu_1/\nu = 0.05$, such that the gap variation at the Γ point is approximately the same as in ZrTe₅²⁵, as shown in Fig. 2e. Because the zone-center phonon carries zero momentum ($q = 0$) it does not mix different Bloch momenta and the Hamiltonian $H(k, t)$ thus remains block diagonal in momentum space. The quantum dynamics simulation can therefore be performed by solving the time-dependent Schrödinger equation separately at each k -point:

$$i\hbar \frac{\partial}{\partial t} |\psi(k, t)\rangle = H(k, t) |\psi(k, t)\rangle. \quad (4)$$

We adopt a discrete-time propagator based on a Trotter decomposition of the state evolution^{60,61}

$$|\psi(k, t + dt)\rangle = e^{-iH(k, t)dt/\hbar} |\psi(k, t)\rangle, \quad (5)$$

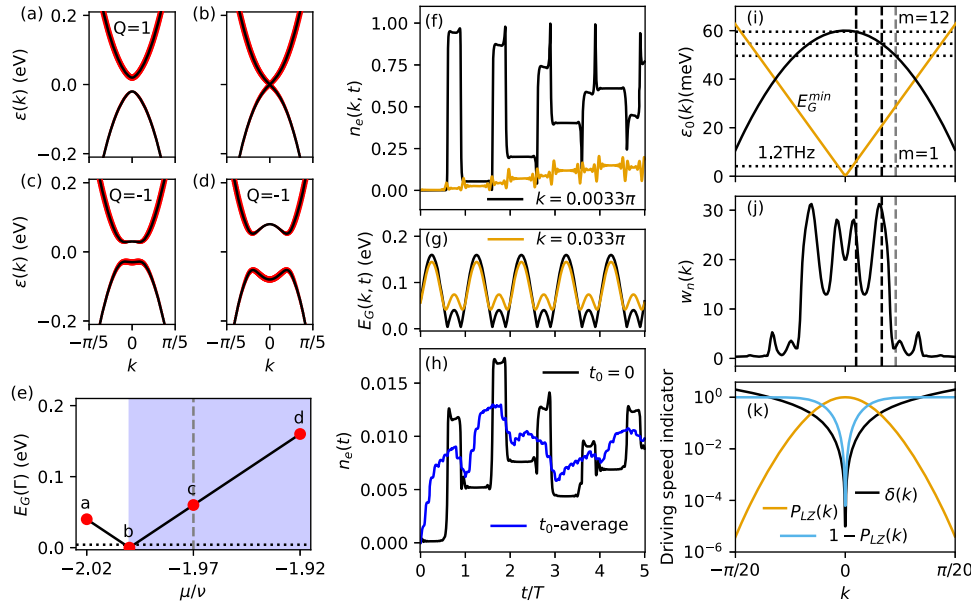


Fig. 2 Toy model results of phonon-induced topological phase transition and carrier excitation dynamics. **a–d** Band structure of the BdG Kitaev chain model with the onsite energy μ to the nearest-neighbor hopping ν ratio $\mu/\nu = -2.02, -2.00, -1.97$, and -1.92 . The red color encodes the projection weight of the band wavefunction on the first basis orbital ($\tau_z = 1$). The topological index $Q = \pm 1$ is also shown. **e** Band gap at the zone center Γ point, $E_G(\Gamma)$, as a function of $\mu/\nu \in [-2.02, -1.92]$. This behavior qualitatively mirrors the behavior of ZrTe₅ system under the A_{1g} Raman phonon modulation²⁵. Red circles indicate μ/ν values in **a–d**. The topological region is highlighted in blue. The vertical dashed line indicates the equilibrium value μ_0 . **f** Time evolution of the excited state population $n_e(k, t)$ for a periodic modulation $\mu(t)/\nu \in [-2.02, -1.92]$ starting at $\mu(t=0) = \mu_0$ for five full cycles. The black line is for $k = 0.0033\pi$ and the orange line for $k = 0.033\pi$. **g** Time evolution of the energy gap $E_G(k, t)$ at $k = 0.0033\pi$ (black) and 0.033π (orange). **h** Excited state population $n_e(t)$. The black curve is for the simulation start time $t_0 = 0$ and the blue one is averaged over 10 runs with t_0 taken from 10 uniformly spaced points in the interval $[0, T)$. **i** The k -point dependence of the offset $\epsilon_0(k)$ ⁹. The bottom horizontal dotted line in **e, i** indicates the energy of the $f_{ph} = 1.2$ THz A_{1g} phonon E_{ph} . The upper three horizontal dotted lines in **i** correspond to $E = mE_{ph}$ with $m = 10, 11$, and 12 . The vertical dashed lines in **i, j** indicate the k -points where $\epsilon_0(k) = mE_{ph}$. The minimal energy gap $E_G^{\min}(k) \equiv \min_{t \in [0, T]} E_G(k, t) = |\Delta(k)|$ over the simulation period is also plotted as orange line for reference. **j** The k -point resolved number density in the excited band, which is defined as $w_n(k) \equiv \int_0^{5T} n_e(k, t) dt / \int_0^{5T} n_e(t) dt$. **k** The k -dependent driving speed indicators: $\delta(k)$ in black line, LZ transition probability $P_{LZ}(k) \equiv e^{-2\pi\delta(k)}$ in orange line, and $1 - P_{LZ}(k)$ in sky blue line.

where the time step $dt \ll T$ is chosen sufficiently small compared to the variation of the onsite energy.

Dynamics simulation results. The simulation starts at time $t = t_0$ and evolves until time $t = t_0 + 5T$ to agree with the experimental situation (see Fig. 1). We monitor the time-dependent excited state population $n_e(t)$, which corresponds to the excited carrier density in the experiment and is tied to the differential emission $\Delta E/E$ that is measured experimentally. In our simulations we obtain $n_e(t) = \frac{1}{2\pi} \int_{-\pi}^{\pi} dk n_e(k, t) \approx \sum_k w_k n_e(k, t)$ as a weighted sum of contributions $n_e(k, t)$ at each k -point in the Brillouin zone $[-\pi, \pi)$. The weight w_k is obtained as $1/N_k$ with N_k the total number of k -points uniformly sampled in the Brillouin zone. Here we define

$$n_e(k, t) = |\langle \psi(k, t) | \psi_c(k, t) \rangle|^2, \quad (6)$$

which is the size of the projection of the one-electron wavefunction $\psi(k, t)$ on the adiabatic conduction band $\psi_c(k, t)$, an eigenstate of $H(k, t)$ with eigenvalue $\epsilon_c(k, t)$. We use a step size $dt = T/1000 = 0.833$ fs and a uniform k -mesh with $N_k = 560$ points, and find that $n_e(t)$ converges to a precision of 10^{-6} .

In Fig. 2f we plot the excited state population $n_e(k, t)$ as a function of time t . We consider five modulation cycles of the onsite energy $\mu(t)$ starting with $t_0 = 0$. The black line represents the data at a momentum point close to the zone center $k = 0.0033\pi$, and the orange line is for momentum $k = 0.033\pi$. The corresponding (instantaneous) energy gap $E_G(k, t)$ at the respective k -points versus t is shown in Fig. 2g. Sharp variations of $n_e(k, t)$ are observed whenever the energy gap is minimal. In total we observe a substantial increase of $n_e(k, t)$ from zero to a finite value at the two representative k -points during the dynamical process. We note that the definition of $n_e(k, t)$ (6) may not be unique. In Supplementary Note 1, we compare the numerical result with that based on an alternative definition, and show that the definition (6) gives more physically reasonable results.

The excited state population per unit cell, $n_e(t)$, is plotted as a black line in Fig. 2h. It shows a similar behavior as $n_e(k, t)$ at the two individual k -points shown in Fig. 2f. By the end of the simulation, $n_e(t = t_0 + 5T)$ has increased from zero to about 0.01. To account for the experimentally unknown initial phase of the coherent phonon oscillation, we also provide results that are averaged over t_0 that is uniformly sampled within the interval $[0, T]$. The averaged results $\bar{n}_e(t) = \frac{1}{10} \sum_{i=0}^9 n_e(t)|_{t_0 = iT}$ are shown in orange in Fig. 2h and also increase from zero to about 0.01 during the simulations.

Discussion of toy model results. The dynamics of the wavefunction at different k -points is completely independent from each other [see Eq. (4)]. The above calculation is thus composed of a collection of independent and periodically-driven two-level systems (TLSs), which resembles the well-known problem of LZS tunneling of a driven TLS in the presence of an avoided crossing^{55,56}. The behavior of the TLS is largely determined by the potential ramp speed (i.e. the oscillation frequency of the drive) and the minimal energy gap in the avoided crossing. While the ramp speed is set by the phonon frequency (1.2 THz), the minimal energy gap $E_G^{\min}(k) \equiv \min_{t \in [0, T]} E_G(k, t)$ and the nature of the diabatic level crossing is strongly k -point dependent. In Fig. 2i, we show the minimal gap E_G^{\min} versus k in the range $k \in [-\pi/20, \pi/20]$. The minimal gap changes almost linearly from zero in the zone center ($k = 0$) to about 60 meV at $k = \pm \pi/20$. For reference, we also plot the 1.2 THz phonon mode energy ($E_{\text{ph}} = 4.96$ meV) as a dotted horizontal line. These findings suggest that the

contribution to the excited carrier density $n_e(t)$ arises from a small part in momentum space around the zone center.

To obtain a more quantitative analysis, we define the following time-averaged and k -resolved excited state density:

$$W_n(k) \equiv \frac{\int_0^{5T} n_e(k, t) dt}{\int_0^{5T} n_e(t) dt}. \quad (7)$$

We plot $W_n(k)$ in Fig. 2j for a simulation with $t_0 = 0$, and find that it peaks in a Γ -centered narrow k -region. Peaks occur in a wider range than naively expected by the condition that $E_G^{\min}(k) \leq E_{\text{ph}}$. We observe several distinct peaks of $W_n(k)$ in this region: the location of the peak closest to Γ -point ($k = 0.004\pi$) and that of the peak furthest away ($k = 0.033\pi$) are close to the k -points chosen for the presentation of $n_e(k, t)$ in (f, g). The peaks can be understood by considering resonance condition of the multi-cycle LZS problem as detailed in the following paragraph.

Although there is no closed form for the solution of the general LZS problem, some analytical understanding can corroborate the numerical results^{55,56}. To facilitate the discussion, we cast the time-dependent Hamiltonian (3) into the following form adopted in references^{55,56}:

$$H(k, t) = -\frac{\Delta(k)}{2} \tau_x - \frac{\epsilon(k, t)}{2} \tau_z, \quad (8)$$

where we apply a $-\pi/2$ rotation around z -axis, and define $\Delta(k) \equiv -4\Delta \sin(k)$, $\epsilon(k, t) \equiv \epsilon_0(k) + A \sin[\omega(t - t_0)]$, with the offset:

$$\epsilon_0(k) = 4\nu \cos(k) + 2\mu_0, \quad (9)$$

and the amplitude $A = 2\mu_1$. The level crossing of the diabatic states (eigenstates of τ_z) occurs at $\epsilon(k, t) = 0$, which requires $-0.09\pi \lesssim k \lesssim 0.09\pi$ for the specific parameters of the model we set. Since the occupation probability of the upper adiabatic state is known to be negligibly small if no diabatic level crossing occurs^{55,56}, this is consistent with the narrow k -range with significant electron population transfer as shown in Fig. 2j. The minimal energy gap between the two adiabatic (i.e. instantaneous) levels reads $E_G^{\min}(k) = |\Delta(k)| = 4\Delta |\sin k|$. It is reached simultaneously with the diabatic state level crossing, and shows a linear behavior at small k as plotted in Fig. 2i. As detailed in references^{55,56}, one can obtain an approximate analytic solution of the LZS problem, in the slow and the fast-passage limits. These limits are characterized by the dimensionless parameter $\delta(k) \equiv [\Delta(k)]^2/[4\nu(k)]$, which characterizes the ratio of the minimal gap $|\Delta(k)|$ and the velocity $v(k) \equiv \frac{\partial \epsilon(k, t)}{\partial t}|_{t_c: \epsilon(k, t)=0} =$

$A\omega \sqrt{1 - [\epsilon_0(k)/A]^2}$ at the minimal gap. The velocity is finite and only weakly varying in the region of interest close the $k = 0$ before it rapidly drops to zero as $k \rightarrow 0.09\pi$. As a result, we find $\delta(k) \propto k^2$ at small k and $\delta = 1$ at $k_1 \approx 0.03\pi$ (see Fig. 2 (k)). In terms of this parameter, the LZ transition probability for a single passage reads $P_{\text{LZ}}(k) \equiv e^{-2\pi\delta(k)}$. In the fast-passage limit at $k \ll k_1$, we have $\delta(k) \ll 1$ and $1 - P_{\text{LZ}}(k) \ll 1$; while in the slow-passage limit, we have $\delta(k) \gg 1$ and $P_{\text{LZ}}(k) \ll 1$. In Fig. 2k we plot these driving speed indicators in the k -region with significant excited state occupation. The fast-passage regime extends from the Γ -point ($k = 0$), where the minimal gap vanishes, roughly to the position of the first peak of $W_n(k)$ at $k = 0.0033\pi$ [see Fig. 2k], where $\delta(k) \lesssim 0.01$ and $1 - P_{\text{LZ}}(k) \lesssim 0.06$. The resonance condition in the diabatic regime reads $\epsilon_0(k) = m\omega$ with integer m . This condition is fulfilled at $k = 0.005\pi$ for $m = 12$ and at $k = 0.017\pi$ for $m = 11$ as shown in by the black vertical dashed lines in Fig. 2i, which explains the two dominant peaks seen in Fig. 2j. Note that we have $\delta(k = 0.017\pi) = 0.26$ and $1 - P_{\text{LZ}}(k = 0.017\pi) = 0.81$, which

implies that $k = 0.017\pi$ is near the crossover from fast to slow passage. In fact, the resonance condition with $m = 10$ gives $k = 0.023\pi$ as shown by a gray vertical dashed line in Fig. 2i, which is off from the peaks in Fig. 2j due to being located close to the crossover region with $\delta(k = 0.023\pi) = 0.48$ and $1 - P_{LZ}(k = 0.023\pi) = 0.95$. At larger $k_1 \approx 0.03\pi$, the crossover from fast to slow passage occurs and one needs to use a more general resonance condition (see Eq. (56) in Ref. ⁵⁶). Finally, for $\pi/20 \leq k \leq 0.09\pi$ and beyond the slow-passage regime is reached, where we find a small adiabatic state probability. The resonance condition in the adiabatic regime reads $\frac{2A}{\pi\omega} = m$ with integer m , which is not exactly fulfilled for our choice of parameters $\frac{2A}{\pi\omega} = 12.8$. One should also take into account that the dynamics only involves five LZS oscillations due to damping effects in experiments, which limits the total transfer into the upper adiabatic state (even on resonance) when $P_{LZ} \ll 1$. We conclude that the majority of the excited state population dynamics in our model occurs in the fast-passage region and the crossover regime between the fast and the slow-passage limits, and that the main peaks can be understood as arising from resonances in the diabatic regime.

To summarize, our analysis demonstrates the crucial role of the phonon-induced topological band closing for carrier excitation. This creates a finite momentum space volume where effective TLSs experience an avoided level crossing with a sufficiently small band gap such that carriers can be excited through LZS tunneling.

First-principles quantum dynamics simulations

Model and ab initio simulation method. To gain a more material-specific understanding of the carrier excitation dynamics of the phonon-modulated ZrTe₅ system, we carry out first-principles simulations based on time-dependent Schrödinger equation with DFT basis functions. The time-dependence of the KS Hamiltonian $\hat{\mathcal{H}}_0(t)$ is encoded in the ionic trajectory $\mathbf{R}(t)$ that is set by the A_{1g} coherent phonon. In the implementation of DFT for periodic systems one often adopts a basis set with large dimension, such as plane waves. This renders a direct manipulation of the DFT Hamiltonian $\hat{\mathcal{H}}_0(t)$ cumbersome. Note that $\hat{\mathcal{H}}_0(t)$ generally covers higher-energy unoccupied states and deeper occupied states, which are likely irrelevant for the carrier excitation dynamics in phonon-modulated ZrTe₅, which we expect to be dominated by states close to the chemical potential. Standard tight-binding downfolding approaches, such as maximally localized Wannier function⁶² and quasi-atomic minimal basis-set orbitals method^{63,64}, can be useful; but the downfolding calculation for many snapshots along the trajectory $\mathbf{R}(t)$ in the simulation time period can be time-consuming, and the time-dependence of the downfolded orbitals introduces additional complexity. Here we adopt an alternative representation where the component of the dynamical electronic state $|\Psi(t)\rangle = \otimes_{\mathbf{k}} |\Psi(\mathbf{k}, t)\rangle$ is approximated as a linear combination of N_b adiabatic states $\{|\Phi_i(\mathbf{k}, t)\rangle\}$ generalized to a generic \mathbf{k} -point from Ref. ^{65,66}:

$$|\Psi(\mathbf{k}, t)\rangle = \sum_{i=1}^{N_b} c_i(\mathbf{k}, t) |\Phi_i(\mathbf{k}, t)\rangle, \quad (10)$$

where $|\Phi_i(\mathbf{k}, t)\rangle \equiv \prod_{\mu \in S_i} \phi_{\mu}^{\dagger}(\mathbf{k}, t) |0\rangle$ is a noninteracting single Slater determinant state defined by a set S_i of occupied KS orbitals $\phi_{\mu}(\mathbf{k}, t)$, which satisfies $\hat{\mathcal{H}}_0(\mathbf{k}, \mathbf{R}(t)) |\phi_{\mu}(\mathbf{k}, t)\rangle = \epsilon_{\mu}(\mathbf{k}, t) |\phi_{\mu}(\mathbf{k}, t)\rangle$. Here the crystal momentum \mathbf{k} is conjugate to the position vector of the simulation unit cell.

The propagation of $|\Psi(\mathbf{k}, t)\rangle$ is encoded in the time-dependent complex amplitudes $c_i(\mathbf{k}, t)$ and the adiabatic states $|\Phi_i(\mathbf{k}, t)\rangle$. Substituting Eq. (10) into the time-dependent Schrödinger

equation leads to the equation of motion (EOM) of the amplitudes

$$i\hbar \frac{\partial c_i(\mathbf{k}, t)}{\partial t} = \sum_{j=1}^{N_b} H_{ij}(\mathbf{k}, t) c_j(\mathbf{k}, t). \quad (11)$$

The vibronic Hamiltonian is given by

$$H_{ij}(\mathbf{k}, t) = \epsilon_i(\mathbf{k}, t) \delta_{ij} - i\hbar d_{ij}(\mathbf{k}, t). \quad (12)$$

Here, we define $\epsilon_i(\mathbf{k}, t) = \sum_{\mu \in S_i} \epsilon_{\mu}(\mathbf{k}, t)$. The complex nonadiabatic coupling (NAC) coefficient between a pair of distinct states $\{|\Phi_i\rangle, |\Phi_j\rangle\}$ is given by $d_{ij} = \langle \Phi_i | \frac{\partial}{\partial t} | \Phi_j \rangle$, which is nonzero only if there is exactly one distinct occupied KS orbital between $|\Phi_i\rangle$ and $|\Phi_j\rangle$ due to the single Slater determinant nature^{67,68}. The NAC can be conveniently evaluated using the finite-difference method⁶⁷:

$$d_{ij}(\mathbf{k}, t) \approx \frac{1}{2dt} \left(\langle \Phi_i(\mathbf{k}, t) | \Phi_j(\mathbf{k}, t + dt) \rangle - \langle \Phi_i(\mathbf{k}, t + dt) | \Phi_j(\mathbf{k}, t) \rangle \right), \quad (13)$$

which is completely determined by the state overlap matrix between consecutive time steps.

Technical details of the simulation. The computational complexity of the simulation is tied to the number N_b of adiabatic states that are used in Eq. (10). The Raman A_{1g} phonon in ZrTe₅ has a frequency of 1.2 THz, which is one order of magnitude smaller than the equilibrium band gap. We can thus truncate the expansion at the level of single-electron excitations between low energy bands. We include configurations with one electron excited from the top valence band to one of the four lowest conduction bands. We thus keep $N_b = 5$ adiabatic states $\Phi_i(\mathbf{k}, t)$ in the expansion at each \mathbf{k} -point. Each Φ_i differs by exactly one occupied KS orbital, which therefore can also be labelled by the same index i , with $i = 1$ corresponding to the top valence band, and $i = 2 \dots N_b$ to the conduction bands in ascending order of energy. The vibronic Hamiltonian (12) can be simplified by setting $\epsilon_i(\mathbf{k}, t) = \epsilon_i(\mathbf{k}, t)$ as a rigid potential shift. The evaluation of the NAC (13) can also be reduced to

$$d_{ij}(\mathbf{k}, t) \approx \frac{1}{2dt} \left(\langle \phi_i(\mathbf{k}, t) | \phi_j(\mathbf{k}, t + dt) \rangle - \langle \phi_i(\mathbf{k}, t + dt) | \phi_j(\mathbf{k}, t) \rangle \right), \quad (14)$$

which depends only on the N_b KS orbitals that are kept at each \mathbf{k} -point.

The EOM (11) assumes the continuity of the time dependent basis $|\Phi_i(\mathbf{k}, t)\rangle$ with t . Therefore, it is crucial to fix the phase degree of freedom of the KS orbitals $\phi_i(\mathbf{k}, t)$. This can be achieved by consecutively applying a phase factor to $\phi_i(\mathbf{k}, t + dt) \rightarrow e^{i\theta} \phi_i(\mathbf{k}, t + dt)$, where the phase $e^{i\theta} \equiv O_i^* / |O_i|$ with $O_i = \langle \phi_i(\mathbf{k}, t) | \phi_i(\mathbf{k}, t + dt) \rangle$ is determined by the overlap with the same orbital at the previous time step. Additional complexity of the dynamics simulations originates from the presence of time-reversal and inversion symmetry, which renders every band doubly degenerate, and strong spin-orbit coupling in ZrTe₅. The ambiguity in the doubly degenerate bands can be partially fixed by choosing a S_z -gauge such that the 2×2 spin S_z matrix becomes diagonal in each doubly degenerate manifold via a unitary transformation. Numerically, we find that the S_z gauge transformation is not sufficient to guarantee the orbital continuity along the dynamical path. Therefore, we propose the following overlap gauge correction to better address the band degeneracy problem. The simulation starts with orbitals in the S_z -gauge, and apply unitary transformation in each doubly degenerate manifold in all following time steps, such that each rotated orbital $\phi_i(\mathbf{k}, t + dt)$

has maximal overlap with the same one at the previous step. This is achieved by diagonalizing a series of 2×2 matrices $P_{rs}^{(j)} = \langle \phi_r^{(j)}(\mathbf{k}, t + dt) | \hat{P}_j | \phi_s^{(j)}(\mathbf{k}, t + dt) \rangle$ with $\hat{P}_j = |\phi_1^{(j)}(\mathbf{k}, t)\rangle \langle \phi_1^{(j)}(\mathbf{k}, t)|$. Here $r, s \in [1, 2]$ run through the two orbitals in the j th degenerate doublet. The diagonalization gives two eigenvectors, where one has a nonzero eigenvalue and is assigned to the first orbital of the j th doublet. The other eigenvector has zero eigenvalue, and is assigned to the second orbital in the doublet. Following this procedure, we numerically find that the self-overlap of each wavefunction at consecutive time steps always remains above 99.99%. The band index exchange between different degenerate doublets, which can be detected by checking the overlap between wavefunctions at consecutive time steps, is not observed in the simulations reported here. In Supplementary Note 2, we compare the NAC amplitudes evaluated with and without phase correction to demonstrate the significance of properly fixing the gauge and phase degrees of freedom.

First-principles quantum dynamics simulation results. The analysis of the one-dimensional (1D) toy model results shows that the main contribution to the carriers in the excited band resulted from LZS tunneling in a narrow region of momentum space around the zone center $k \in [-\pi/20, \pi/20]$. Expecting a similar behavior for the realistic 3D model of ZrTe₅, we use a dense $360 \times 360 \times 120$ uniform \mathbf{k} -grid covering the full Brillouin zone for the following dynamics simulations and use a shift of $\Delta = \frac{0.5}{360}(\mathbf{b}_1 + \mathbf{b}_2) + \frac{0.5}{120}\mathbf{b}_3$ from the Γ -point for each \mathbf{k} -point. Here, \mathbf{b}_i are the reciprocal basis vectors. The center-shifted \mathbf{k} -mesh therefore excludes the Γ -point, where the band gap closes at certain times and additional gauge correction is otherwise needed.

In Fig. 3a we present the excited state population $n_e(i, \mathbf{k}, t)$ as a function of simulation time t for five phonon cycles, starting at

$t_0 = 0$ with zero phonon displacement. Here we define

$$n_e(i, \mathbf{k}, t) \equiv |c_i(\mathbf{k}, t)|^2, \quad (15)$$

which is equivalent to the definition used in the toy model analysis. At momentum $\mathbf{k} = \mathbf{b}_3/120 + \Delta$ adjacent to the zone center, an electron is gradually excited from the top valence band ($i = 1$) to the two lowest conduction bands ($i = 2, 3$) due to nonadiabatic effects. The complex NAC amplitude $\hbar d_{13}(\mathbf{k}, t)$ between the 1st and 3rd bands at the same \mathbf{k} -point is plotted in Fig. 3b. The yellow line denotes the real part and the red line the imaginary part. The line width indicates the numerical noise, which is found to have negligible impact on the state population dynamics. The maximal difference in the dynamical state populations from the simulation using the (noisy) NAC amplitudes versus using smoothed data via application of a Savitzky-Golay filter is only about 10^{-3} . Clearly, Fig. 3a, b shows that a sharp transition of the state population n_e occurs at the peaks of the NAC. This also coincides with a minimum of the band gap, $E_G = \varepsilon_2(\mathbf{k}, t) - \varepsilon_1(\mathbf{k}, t)$, as indicated by the blue shading in the background of Fig. 3b. We note that $d_{12}(\mathbf{k}, t)$ has a similar time-dependence as $d_{13}(\mathbf{k}, t)$ [both bands have degenerate energies $\varepsilon_2(\mathbf{k}, t) = \varepsilon_3(\mathbf{k}, t)$], yet with slightly larger amplitude. This difference in the NAC induces a larger electron occupancy in the $i = 2$ band compared to the one with $i = 3$, as shown in Fig. 3a. In contrast, the NACs from $i = 1$ to $i = 4, 5$ are smaller by more than one order of magnitude, resulting in negligibly small carrier excitations to these bands, $n_e(i, \mathbf{k}, t) < 10^{-6}$ for $i = 4, 5$.

The first-principles dynamics simulations allow for a direct and quantitative comparison to experiment. First, in Fig. 3c we show the excited state carrier density, $n_e(t) = \sum_{\mathbf{k}} w_{\mathbf{k}} \sum_{i=2}^3 n_e(i, \mathbf{k}, t)$ as a function of time t . It increases from zero to about $n_e(t = 5T) \approx 2.4 \times 10^{16} \text{ cm}^{-3}$ at the end of the simulation $t = 5T$ and exhibits qualitatively similar sharp transitions near dynamical band gap minimum as the momentum resolved quantity in

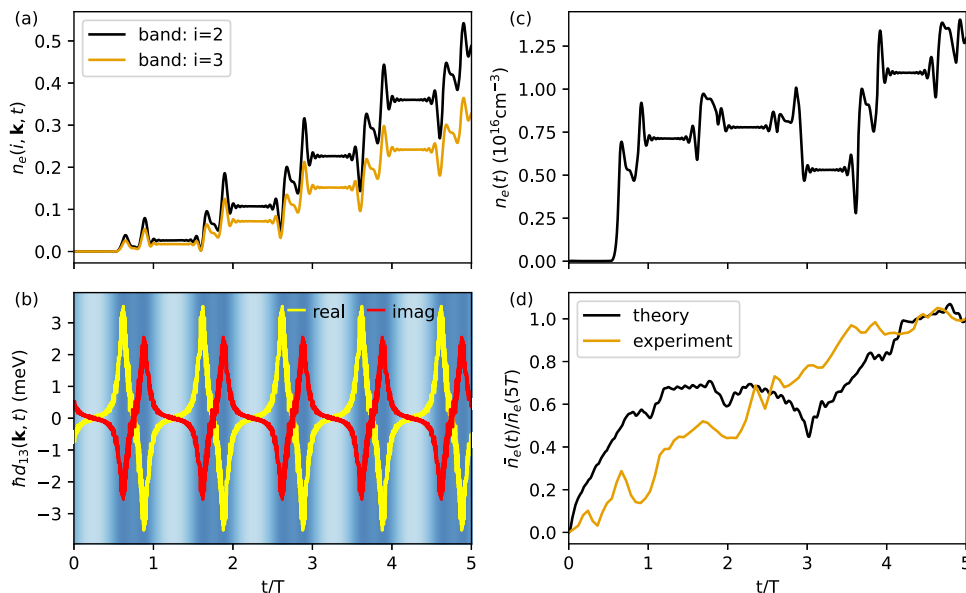


Fig. 3 Carrier excitation dynamics of phonon-modulated ZrTe₅ system from first-principles simulations. **a** Occupancy of the two lowest-energy conduction bands, $n_e(i, \mathbf{k}, t)$ with $i = 2, 3$, as a function of simulation time t for 5 phonon periods starting with $t_0 = 0$ (the equilibrium configuration with zero phonon displacement) at $\mathbf{k} = \mathbf{b}_1/720 + \mathbf{b}_2/720 + \mathbf{b}_3/80$. Here $(\mathbf{b}_1, \mathbf{b}_2, \mathbf{b}_3)$ are the reciprocal primitive vectors (see Methods for details). **b** Time-dependence of the complex nonadiabatic coupling amplitude $\hbar d_{13}(\mathbf{k}, t)$ between the top valence band ($i = 1$) and lowest conduction band ($i = 3$) at the same \mathbf{k} -point as **a**, with real part in yellow and imaginary part in red. The background dark blue to light blue indicates a band gap, $E_G = \varepsilon_2(\mathbf{k}, t) - \varepsilon_1(\mathbf{k}, t)$, varying from 27 meV to 132 meV. **c** The total excited states population $n_e(t)$ integrated over the Brillouin zone as a function of t for the simulation starting with $t_0 = 0$. **d** The time-evolution of normalized $\bar{n}_e(t)/\bar{n}_e(5T)$ (black line), where $\bar{n}_e(t)$ is the total excited states population $n_e(t)$ averaged over simulations starting with t_0 uniformly sampled by 10-points in a phonon period. The normalized experimental carrier density change $\Delta n(t)/\Delta n(5T)$ are also plotted in orange line. We obtain $\bar{n}_e(5T) = 1.2 \times 10^{16} \text{ cm}^{-3}$ from the theoretical simulation, and $\Delta n(5T) = (0.28 \pm 0.12) \times 10^{16} \text{ cm}^{-3}$ estimated from the experiment.

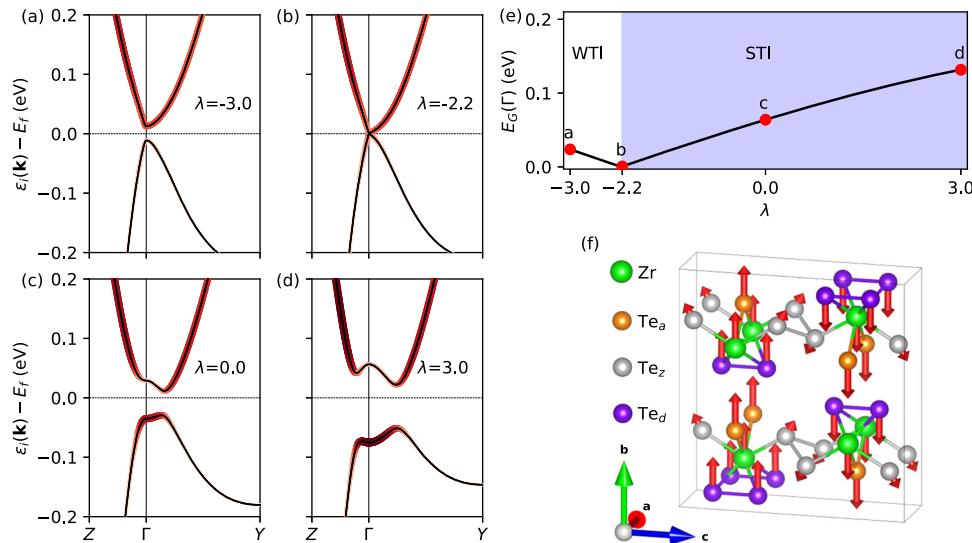


Fig. 4 DFT band structure calculations for the adiabatic topological phase switching induced by the A_{1g} Raman phonon mode in $ZrTe_5$. **a-d** Band structure along \mathbf{k} -path $Z-\Gamma-Y$ with distortion parameter $\lambda = -3.0, -2.2, 0.0$, and 3.0 , respectively. The red color encodes projection weight of 5p-orbitals of Te_d along the wavefunctions. We define $Z = (0, 0, 0.5)$ and $Y = (-0.5, 0.5, 0)$ in the reciprocal space with basis vectors $(\mathbf{b}_1, \mathbf{b}_2, \mathbf{b}_3)$. **e** Band gap at the zone center, $E_G(\Gamma)$, as a function of distortion parameter λ . Here $\lambda = 1$ represented 0.033 \AA displacement for Zr, 0.035 \AA for Te_d , 0.032 \AA for Te_a , and 0.017 \AA for Te_z ²⁵. Red circles indicate the λ values for **a-d**. The strong topological insulator (STI) region is highlighted in blue and weak topological insulator (WTI) region in white, with boundary line indicating the Dirac point position. **f** The A_{1g} phonon mode in the conventional cell of $ZrTe_5$. Green spheres represent Zr atoms, orange spheres for apical Te atoms (Te_a), silver spheres for zigzag Te atoms (Te_z), and purple spheres for dimerized Te atoms (Te_d). The arrows indicate the atomic displacement vectors of the A_{1g} mode.

Fig. 3a. Within the $360 \times 360 \times 120$ uniform \mathbf{k} -mesh of the Brillouin zone, we find that the dominant contributions come from $\mathbf{k} = \frac{l}{360}\mathbf{b}_1 + \frac{m}{360}\mathbf{b}_2 + \frac{n}{120}\mathbf{b}_3 + \Delta$ with $l, m, n = 0, \pm 1, \pm 2, -3$. Next, we account for the fact that in pump-probe experiments, the time-trace of differential transmission is obtained as an average over multiple runs and $ZrTe_5$ samples exhibit some degree of electronic heterogeneity and nanostrip junctions, as observed in the THz nanoimaging⁴⁸. To capture these phenomena on average, we define $\bar{n}_e(t) = \frac{1}{10} \sum_{i=0}^9 n_e(t)|_{t_0 = \frac{i}{10}T}$, which is an average over simulations at 10 different starting times. In Fig. 3d we directly compare the time-dependence of a normalized $\bar{n}_e(t)/\bar{n}_e(t=5T)$ (black), to the experimental data $\Delta n(t)/\Delta n(t=5T)$ (orange). Both curves exhibit a similar growth pattern of the carrier density over time, and we also find the carrier density at the end of the simulation $\bar{n}_e(t=5T) \approx 2.4 \times 10^{16} \text{ cm}^{-3}$ to be in good agreement with the one estimated from experiment $\Delta n(5T) = (0.28 \pm 0.12) \times 10^{16} \text{ cm}^{-3}$, considering that there is electronic heterogeneity present in the experimental $ZrTe_5$ sample⁴⁸. The numerical estimation of $n_e(t=5T)$ and $\bar{n}_e(t=5T)$ reported here also includes a factor of 2 to take into account the double degeneracy of the top valence band in $ZrTe_5$ system.

Conclusions

We report detailed first-principle and effective model simulations of the carrier excitation dynamics in coherent phonon-modulated $ZrTe_5$. Our results shed new light on recent pump-probe experiments²⁵ by providing a clear intuitive explanation of the experimental results. Both first-principle and effective model calculations reveal the importance of the phonon-induced topological phase transition in $ZrTe_5$ and the associated closing of the bulk gap for the observed excitation of carriers. We show that the excitations occur via Landau-Zener-Stückelberg tunneling in a series of time-dependent avoided level crossings of Bloch states located in a narrow region of momentum space around the zone center. Our detailed time-dependent Schrödinger equation

simulations further show that the dominant tunneling occurs between the highest valence band and the lowest doubly degenerate conduction bands, while excitations to the next higher bands are negligible due to small transition matrix elements. We predict that the carrier density increases gradually with time and reaches a final value of $2.4 \times 10^{16} \text{ cm}^{-3}$ at $t = 5T$ when phonon coherence is lost in the experiment. These results are in good quantitative agreement with experiment. Our work thus demonstrates that the coherent charge excitation process in topological quantum materials such as $ZrTe_5$ can be understood and predicted quantitatively by first-principles quantum dynamics simulations.

Methods

First-principles total energy and electronic-structure calculations for $ZrTe_5$ are based on DFT with the exchange correlation functional in generalized gradient approximation parametrized by Perdew, Burke, and Ernzerhof (PBE)⁶⁹. Van der Waals interaction is included by Grimme's damped atom-pairwise dispersion corrections (D2)⁷⁰. The calculations are performed using the Vienna Ab initio Simulation Package (VASP)⁷¹. We use a plane-wave cutoff energy of 230 eV and include spin-orbit coupling for all the calculations. The phonon modes are calculated using the finite displacement approach as implemented in Phonopy⁷². Specifically, we use the primitive unit cell of experimental structure ($a = 3.987 \text{ \AA}$, $b = 14.502 \text{ \AA}$, and $c = 13.727 \text{ \AA}$)⁷³. The primitive vectors are $\mathbf{a}_1 = (1.994, -7.251, 0) \text{ \AA}$, $\mathbf{a}_2 = (1.994, 7.251, 0) \text{ \AA}$, and $\mathbf{a}_3 = (0, 0, 13.727) \text{ \AA}$. The corresponding reciprocal primitive vectors are $\mathbf{b}_1 = (0.251, -0.069, 0)2\pi \text{ \AA}^{-1}$, $\mathbf{b}_2 = (0.251, 0.069, 0)2\pi \text{ \AA}^{-1}$, and $\mathbf{b}_3 = (0, 0, 0.073)2\pi \text{ \AA}^{-1}$. Highly accurate wavefunctions at specific \mathbf{k} -points are generated for NAC calculations by setting an energy convergence criterion to 10^{-9} eV and requiring a minimum of 20 electronic steps.

To be self-contained, we present the key DFT band structure calculation results for the description of the A_{1g} phonon-induced

adiabatic topological phase transition observed in ZrTe_5 system as reported in Ref. ²⁵. Under the modulation of the A_{1g} eigenmode as plotted in Fig. 4f, the band gap $E_G(\Gamma)$ at zone center closes at distortion parameter $\lambda = -2.2$ as shown in Fig. 4e, implying a topological phase transition along the dynamical path. This is confirmed by the band structure analysis and topological invariant index calculation²⁵. In Fig. 4a–d, we plot the band structure along high-symmetry k -path $Z - \Gamma - Y$ at phonon distortion parameter $\lambda = -3.0, -2.2, 0, 3.0$, decorated with red color indicating the Te_d $5p$ -orbital weight. Band inversion clearly occurs when λ passes through $\lambda = -2.2$ the Dirac point. For $\lambda < -2.2$, the adiabatic state of the system is in WTI, and switches to STI for $\lambda > -2.2$.

Data availability

All the data to generate the figures are available at figshare⁷⁴. Data supporting the calculations are available together with the codes at figshare⁷⁵. All other data are available from the corresponding authors on reasonable request.

Code availability

All the computer codes developed and used in this work are available open-source at figshare⁷⁵.

Received: 5 May 2023; Accepted: 4 October 2023;

Published online: 14 October 2023

References

1. Först, M. et al. Nonlinear phononics as an ultrafast route to lattice control. *Nat. Phys.* **7**, 854 (2011).
2. Merlin, R. Generating coherent THz phonons with light pulses. *Solid State Commun.* **102**, 207 (1997).
3. Dhar, L., Rogers, J. A. & Nelson, K. A. Time-resolved vibrational spectroscopy in the impulsive limit. *Chem. Rev.* **94**, 157 (1994).
4. Basov, D., Averitt, R. & Hsieh, D. Towards properties on demand in quantum materials. *Nat. Mater.* **16**, 1077 (2017).
5. Mankowsky, R., Först, M. & Cavalleri, A. Non-equilibrium control of complex solids by nonlinear phononics. *Rep. Prog. Phys.* **79**, 064503 (2016).
6. de la Torre, A. et al. Colloquium: Nonthermal pathways to ultrafast control in quantum materials. *Rev. Mod. Phys.* **93**, 041002 (2021).
7. Disa, A. S., Nova, T. F. & Cavalleri, A. Engineering crystal structures with light. *Nat. Phys.* **17**, 1087 (2021).
8. Stremoukhov, P. et al. Phononic manipulation of antiferromagnetic domains in nio. *New J. Phys.* **24**, 023009 (2022).
9. Stupakiewicz, A. et al. Ultrafast phononic switching of magnetization. *Nat. Phys.* **17**, 489 (2021).
10. Nova, T. F. et al. An effective magnetic field from optically driven phonons. *Nat. Phys.* **13**, 132 (2017).
11. Rini, M. et al. Control of the electronic phase of a manganite by mode-selective vibrational excitation. *Nature* **449**, 72 (2007).
12. Caviglia, A. D. et al. Ultrafast strain engineering in complex oxide heterostructures. *Phys. Rev. Lett.* **108**, 136801 (2012).
13. Horstmann, J. G. et al. Coherent control of a surface structural phase transition. *Nature* **583**, 232 (2020).
14. Song, B. et al. Ultrafast martensitic phase transition driven by intense terahertz pulses. *Ultrafast Sci.* **3**, 0007 (2023).
15. Kaiser, S. et al. Optically induced coherent transport far above T_c in underdoped $\text{YBa}_2\text{Cu}_3\text{O}_{6+\delta}$. *Phys. Rev. B* **89**, 184516 (2014).
16. Hu, W. et al. Optically enhanced coherent transport in $\text{YBa}_2\text{Cu}_3\text{O}_{6.5}$ by ultrafast redistribution of interlayer coupling. *Nat. Mater.* **13**, 705 (2014).
17. Mankowsky, R. et al. Nonlinear lattice dynamics as a basis for enhanced superconductivity in $\text{YBa}_2\text{Cu}_3\text{O}_{6.5}$. *Nature* **516**, 71 (2014).
18. Mitran, M. et al. Possible light-induced superconductivity in $\text{K}_3\text{C}_6\text{O}$ at high temperature. *Nature* **530**, 461 (2016).
19. Garate, I. Phonon-induced topological transitions and crossovers in dirac materials. *Phys. Rev. Lett.* **110**, 046402 (2013).
20. Saha, K. & Garate, I. Phonon-induced topological insulation. *Phys. Rev. B* **89**, 205103 (2014).
21. Kim, J. & Jhi, S.-H. Topological phase transitions in group iv-ii semiconductors by phonons. *Phys. Rev. B* **92**, 125142 (2015).
22. Wang, L.-L. et al. Phonon-induced topological transition to a type-II Weyl semimetal. *Phys. Rev. B* **95**, 165114 (2017).
23. Weber, C. P. et al. Using coherent phonons for ultrafast control of the dirac node of SrMnSb_2 . *Phys. Rev. B* **98**, 155115 (2018).
24. Sie, E. J. et al. An ultrafast symmetry switch in a weyl semimetal. *Nature* **565**, 61 (2019).
25. Vaswani, C. et al. Light-driven Raman coherence as a nonthermal route to ultrafast topology switching in a dirac semimetal. *Phys. Rev. X* **10**, 021013 (2020).
26. Luo, L. et al. A light-induced phononic symmetry switch and giant dissipationless topological photocurrent in ZrTe_5 . *Nat. Mater.* **20**, 329 (2021).
27. Wang, L.-L. Expansive open fermi arcs and connectivity changes induced by infrared phonons in ZrTe_5 . *Phys. Rev. B* **103**, 075105 (2021).
28. Yang, X. et al. Light control of surface–bulk coupling by terahertz vibrational coherence in a topological insulator. *npj Quantum Mater.* **5**, 13 (2020).
29. Yang, X. et al. Terahertz-light quantum tuning of a metastable emergent phase hidden by superconductivity. *Nat. Mater.* **17**, 586 (2018).
30. Prezhdo, O. V. Modeling non-adiabatic dynamics in nanoscale and condensed matter systems. *Acc. Chem. Res.* **54**, 4239 (2021).
31. Lindh, R. and González, L., <https://doi.org/10.1002/9781119417774> *Quantum Chemistry and Dynamics of Excited States: Methods and Applications* (John Wiley & Sons, 2020).
32. Nelson, T. R. et al. Non-adiabatic excited-state molecular dynamics: Theory and applications for modeling photophysics in extended molecular materials. *Chem. Rev.* **120**, 2215 (2020).
33. Curchod, B. F. & Martínez, T. J. Ab initio nonadiabatic quantum molecular dynamics. *Chem. Rev.* **118**, 3305 (2018).
34. Caruso, F. & Zacharias, M. Quantum theory of light-driven coherent lattice dynamics. *Phys. Rev. B* **107**, 054102 (2023).
35. Subedi, A., Cavalleri, A. & Georges, A. Theory of nonlinear phononics for coherent light control of solids. *Phys. Rev. B* **89**, 220301 (2014).
36. Gu, M. & Rondinelli, J. M. Nonlinear phononic control and emergent magnetism in mott insulating titanates. *Phys. Rev. B* **98**, 024102 (2018).
37. Raines, Z. M., Stanev, V. & Galitski, V. M. Enhancement of superconductivity via periodic modulation in a three-dimensional model of cuprates. *Phys. Rev. B* **91**, 184506 (2015).
38. Komnik, A. & Thorwart, M. BCS theory of driven superconductivity. *Eur. Phys. J. B* **89**, 244 (2016).
39. Knap, M., Babadi, M., Refael, G., Martin, I. & Demler, E. Dynamical Cooper pairing in nonequilibrium electron-phonon systems. *Phys. Rev. B* **94**, 214504 (2016).
40. Patel, A. A. & Eberlein, A. Light-induced enhancement of superconductivity via melting of competing bond-density wave order in underdoped cuprates. *Phys. Rev. B* **93**, 195139 (2016).
41. Kennes, D. M., Wilner, E. Y., Reichman, D. R. & Millis, A. J. Transient superconductivity from electronic squeezing of optically pumped phonons. *Nat. Phys.* **13**, 479 (2017).
42. Babadi, M., Knap, M., Martin, I., Refael, G. & Demler, E. Theory of parametrically amplified electron-phonon superconductivity. *Phys. Rev. B* **96**, 014512 (2017).
43. Mazza, G. & Georges, A. Nonequilibrium superconductivity in driven alkali-doped fullerides. *Phys. Rev. B* **96**, 064515 (2017).
44. Murakami, Y., Tsuji, N., Eckstein, M. & Werner, P. Nonequilibrium steady states and transient dynamics of conventional superconductors under phonon driving. *Phys. Rev. B* **96**, 045125 (2017).
45. Sentef, M. A. Light-enhanced electron-phonon coupling from nonlinear electron-phonon coupling. *Phys. Rev. B* **95**, 205111 (2017).
46. Schütt, M., Orth, P. P., Levchenko, A. & Fernandes, R. M. Controlling competing orders via nonequilibrium acoustic phonons: Emergence of anisotropic effective electronic temperature. *Phys. Rev. B* **97**, 035135 (2018).
47. Luo, L. et al. Quantum coherence tomography of light-controlled superconductivity. *Nat. Phys.* **19**, 201 (2023).
48. Kim, R. H. et al. Terahertz nano-imaging of electronic strip heterogeneity in a dirac semimetal. *ACS Photon.* **8**, 1873 (2021).
49. Liu, Z. et al. Ultrafast control of excitonic rashba fine structure by phonon coherence in the metal halide perovskite $\text{CH}_3\text{NH}_3\text{PbI}_3$. *Phys. Rev. Lett.* **124**, 157401 (2020).
50. Liu, Z. et al. Coherent band-edge oscillations and dynamic longitudinal-optical phonon mode splitting as evidence for polarons in perovskites. *Phys. Rev. B* **101**, 115125 (2020).
51. Landau, L. D. Zur Theorie der Energieübertragung. II. *Phys. Z. Sowjetunion* **2**, 46 (1932).
52. Zener, C. Non-adiabatic crossing of energy levels. *Proc. R. Soc. London, Ser. A* **137**, 696 (1932).
53. Stückelberg, E. C. G. Theorie der unelastischen Stöße zwischen Atomen. *Helv. Phys. Acta* **5**, 369 (1932).
54. Majorana, E. Atomi orientati in campo magnetico variabile. *Nuovo Cim.* **9**, 43 (1932).

55. Shevchenko, S. N., Ashhab, S. & Nori, F. Landau–Zener–Stückelberg interferometry. *Phys. Rep.* **492**, 1 (2010).
56. Ivakhnenko, V., Shevchenko, S. N. & Nori, F. Nonadiabatic Landau–Zener–Stückelberg–Majorana transitions, dynamics, and interference. *Phys. Rep.* **995**, 1 (2023).
57. Akhmerov, A. et al. Topology in Condensed Matter: Tying Quantum Knots, <https://topocondmat.org/>.
58. Aryal, N., Jin, X., Li, Q., Tsvetlik, A. M. & Yin, W. Topological phase transition and phonon-space dirac topology surfaces in ZrTe_5 . *Phys. Rev. Lett.* **126**, 016401 (2021).
59. Holstein, T. Studies of polaron motion: Part I. the molecular-crystal model. *Ann. Phys.* **8**, 325 (1959).
60. Trotter, H. F. On the product of semi-groups of operators. *Proc. Am. Math. Soc.* **10**, 545 (1959).
61. Nielsen, M. A. and Chuang, I. L., <https://doi.org/10.1017/CBO9780511976667> *Quantum Computation and Quantum Information: 10th Anniversary Edition*, 10th ed. (Cambridge University Press, New York, USA, 2011).
62. Marzari, N., Mostofi, A. A., Yates, J. R., Souza, I. & Vanderbilt, D. Maximally localized wannier functions: theory and applications. *Rev. Mod. Phys.* **84**, 1419 (2012).
63. Chan, T.-L. et al. Highly localized quasiatomic minimal basis orbitals for mo from ab initio calculations. *Phys. Rev. B* **76**, 205119 (2007).
64. Qian, X. et al. Quasiatomic orbitals for ab initio tight-binding analysis. *Phys. Rev. B* **78**, 245112 (2008).
65. Granucci, G., Persico, M. & Spighi, G. Surface hopping trajectory simulations with spin-orbit and dynamical couplings. *J. Chem. Phys.* **137**, 22A501 (2012).
66. Li, W., Zhou, L., Prezhdo, O. V. & Akimov, A. V. Spin–orbit interactions greatly accelerate nonradiative dynamics in lead halide perovskites. *ACS Energy Lett.* **3**, 2159 (2018).
67. Hammes-Schiffer, S. & Tully, J. C. Proton transfer in solution: molecular dynamics with quantum transitions. *J. Chem. Phys.* **101**, 4657 (1994).
68. Akimov, A. V. & Prezhdo, O. V. The pyxaid program for non-adiabatic molecular dynamics in condensed matter systems. *J. Chem. Theory Comput.* **9**, 4959 (2013).
69. Perdew, J. P., Burke, K. & Ernzerhof, M. Generalized gradient approximation made simple. *Phys. Rev. Lett.* **77**, 3865 (1996).
70. Grimme, S. Semiempirical gga-type density functional constructed with a long-range dispersion correction. *J. Comput. Chem.* **27**, 1787 (2006).
71. Kresse, G. & Furthmüller, J. Efficient iterative schemes for ab initio total-energy calculations using a plane-wave basis set. *Phys. Rev. B* **54**, 11169 (1996).
72. Togo, A. & Tanaka, I. First principles phonon calculations in materials science. *Scr. Mater.* **108**, 1 (2015).
73. Matkovic, T. & Matkovic, P. Constitutional study of the titanium, zirconium and hafnium tellurides. *Metalurgija (Zagreb)* **31**, 107 (1992).
74. Jiang, T., Orth, P. P., Luo, L., Wang, J., and Yao, Y.-X., Data set and scripts for the analysis and figures of quantum dynamics simulations of ZrTe_5 system, https://figshare.com/articles/dataset/Data_qd_zrte5/23786355, <https://doi.org/10.6084/m9.figshare.23786355> (2023).
75. Yao, Y.-X., CyQuanDyn: coherent phonon-driven quantum dynamics simulation toolkit, <https://figshare.com/articles/software/cyquandyn/23774946>, <https://doi.org/10.6084/m9.figshare.23774946> (2023).

Acknowledgements

This work was supported by the U.S. Department of Energy (DOE), Office of Science, Basic Energy Sciences, Materials Science and Engineering Division, including the grant of computer time at the National Energy Research Scientific Computing Center (NERSC) in Berkeley, California. The research was performed at the Ames National Laboratory, which is operated for the U.S. DOE by Iowa State University under Contract No. DE-AC02-07CH11358.

Author contributions

T.J. performed the DFT and quantum dynamics simulations. Y.X.Y. and T.J. wrote the codes for dynamics simulation and analysis. P.P.O. initiated the effective model simulation and contributed to the analysis of the results. L.L. and J.W. performed the experimental analysis. L.L.W. and F.Z. helped with the DFT calculations and analysis. J.Z., C.Z.W. and K.M.H. provided inputs for the first-principle dynamics simulations. Y.X.Y., T.J. and P.P.O. wrote the paper, with contributions from all the authors. Y.X.Y. supervised the project.

Competing interests

The authors declare no competing interests.

Additional information

Supplementary information The online version contains supplementary material available at <https://doi.org/10.1038/s42005-023-01415-6>.

Correspondence and requests for materials should be addressed to Yong-Xin Yao.

Peer review information *Communications Physics* thanks Chao Lian and the other, anonymous, reviewer(s) for their contribution to the peer review of this work. A peer review file is available.

Reprints and permission information is available at <http://www.nature.com/reprints>

Publisher's note Springer Nature remains neutral with regard to jurisdictional claims in published maps and institutional affiliations.



Open Access This article is licensed under a Creative Commons Attribution 4.0 International License, which permits use, sharing, adaptation, distribution and reproduction in any medium or format, as long as you give appropriate credit to the original author(s) and the source, provide a link to the Creative Commons license, and indicate if changes were made. The images or other third party material in this article are included in the article's Creative Commons license, unless indicated otherwise in a credit line to the material. If material is not included in the article's Creative Commons license and your intended use is not permitted by statutory regulation or exceeds the permitted use, you will need to obtain permission directly from the copyright holder. To view a copy of this license, visit <http://creativecommons.org/licenses/by/4.0/>.

© The Author(s) 2023